An Overset Grid Method for the Study of Reflex Tearing

K.L. Maki, R.J. Braun, T.A. Driscoll
Department of Mathematical Sciences
University of Delaware
Newark, DE 19711
and
P.E. King-Smith
College of Optometry
The Ohio State University
Columbus, OH 43218

May 23, 2008

Abstract

We present an overset grid method to simulate the evolution of human tear film thickness subject to reflex tearing. The free surface evolution is governed by a single fourth-order nonlinear equation derived from lubrication theory with specified film thickness and volume flux at each end. The model arises from considering the limiting case where the surfactant is strongly affecting the surface tension. In numerical simulations, the overset grid is composed of fine boundary grids near the upper and lower eyelids to capture localized capillary thinning referred to as "black lines" and a Cartesian grid covers the remaining domain. Numerical studies are performed on a nonlinear test problem to confirm the accuracy and convergence of the scheme. The computations on the tear film model show qualitative agreement with *in vivo* tear film thickness measurements. Furthermore, the role of the black lines in the presence of tear supply from the lid margins, reflex tearing, was found to be more subtle than a barrier to tear fluid flow between the anterior of the eye and the meniscus at the lid margin. During reflex tearing, tears may flow through the region normally containing the black line and drift down over the cornea under the influence of gravity.

1 Introduction

The human tear film is typically thought of as a multilayer structure encapsulated in a time dependent region playing a vital role in the health and function of the eye. Figure 1 displays the multilayer structure with the first layer (above the cornea) being a potential mucus layer made of gel-forming mucins whose existence is still debated. Next is the aqueous layer consisting primarily of water and commonly thought of as tears. Finally, the lipid layer, which has an outer non-polar layer with polar surfactants at the aqueous/lipid interface, decreases the surface tension and retards water evaporation. The time dependent domain moves in accordance with the blink cycle, comprised of two subsequent parts in this study: the upstroke or opening of the lids, and

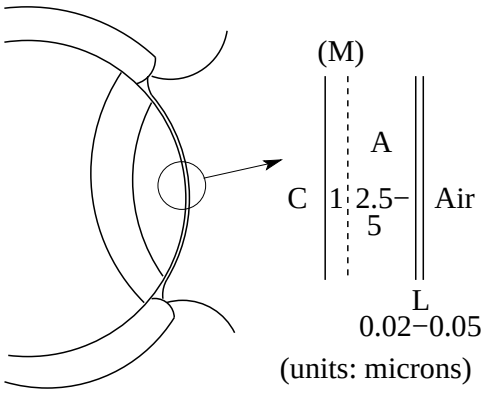

Figure 1: A side view sketch of the pre-corneal tear film where C denotes the cornea, M the possible mucus layer, A the aqueous layer, and L the lipid layer. Possible thickness of each layer in microns is also shown.

the interblink where the lids are kept open. Findings on the phenomenon of reflex tearing indicate that one mechanism triggering the onset of tearing is activation of the sensory nerves in the cornea (Maitchouk *et al.*, 2000). Corneal dehydration, cooling or trauma could be potential triggers, as is the watering of one's eyes from cutting an onion.

In this work, we study the formation and relaxation of the aqueous layer including the phenomenon of reflex tearing. King-Smith *et al.* (2000) published an *in vivo* tear film thickness measurement taken at the center of the cornea in a subject who kept his eyes open for a remarkable 360 seconds; this "six minute man" reported irritation early in the experiment which later disappeared. King-Smith *et al.* (2000) hypothesized that reflex tears were triggered, causing fluid to travel down the cornea and give relief. We aim to verify this hypothesis and identify the mechanism causing the resulting thickness dependence as a function of time. Furthermore, we investigate the difficulty for the tear fluid to break through the "black lines" (local thinning regions near lids) that form during the interblink period. Numerical computations are performed with an overset grid method which can handle localized solution features like the black lines that exist in tear film. The composite grid contains multiple overlapping grids, which allows fine grids to be used only where the tear film thickness is known to change rapidly. This speeds up the computation without degrading accuracy, and facilitates computation on complex domains as discussed below.

We begin with a introduction of human tear film drainage. Pre-corneal tear film drainage after a blink or relaxation has been studied as a Newtonian film in numerous theoretical works (Wong

et al., 1996; Sharma *et al.*, 1998; Braun & Fitt, 2003). During relaxation the tear film evolution is characterized by competing viscous and capillary forces. Using lubrication models with gravity and evaporation absent, all of these works found the minimum point in the film (located near the meniscus) to have a thinning time of t^{α}, where $\alpha = -0.45$ or -0.46. This thinning time yields reasonable results for tear film breakup (also known as rupture) times of pre-corneal tear film in healthy eyes. Braun & Fitt (2003) included the effects of gravity along with evaporation by decoupling the dynamics of the film from the vapor. Therefore, the film itself determines the film flow and evaporation. Given the parameter values for eyes, they found the rate of evaporation to be effectively uniform in space and constant in time. Further, they found gravity redistributes a relatively thick film favoring break-up at the top of the eye.

Jones *et al.* (2005) combined the two stages of evolution, formation and relaxation, using lubrication theory. Considering only upper eyelid motion along with fluxes for the upper lid, two models were studied corresponding to pure tear film or stress-free film (lipid layer has no effect) and a uniformly stretched tear film/air interface (lipid layer contains a strong soluble surfactant). Jones *et al.* (2005) found it to be impossible to form a pre-corneal tear film without influxes from the upper lid during the upstroke. In particular, film breakup occurs in both models near the upper meniscus with only 80% of the cornea exposed. This supports the finding of King-Smith *et al.* (2004), based on cross-sectional area measurements, that supply or exposure of the tear film from under the lids is required to adequately deposit the pre-corneal tear film. The flux function proposed by Jones *et al.* (2005) resulted from exposing a pre-existing constant-thickness fluid layer under the upper lid during the upstroke.

Building upon Jones *et al.* (2005) formation and relaxation models, Heryudono *et al.* (2008) studied the two models described above over multiple blink cycles and partial or half blinks with realistic lid motion functions fit from observed lid motion data. They developed generalized flux boundary conditions, including supply from the lacrimal gland and drainage through the puncta. In their numerical study, better comparisons to *in vivo* measured partial blink data were found when using the uniform stretching limit model coupled with the generalized flux functions.

In this paper, we model the formation and relaxation of the tear film with the uniform stretching limit model. Since we wish to simulate the relaxation or the interblink period for an extended

period of time when compared to the typical blink cycle, the effects of evaporation and gravity will be of importance and hence included. The end fluxes are modified functions previously used by Heryudono *et al.* (2008) with modification to incorporate reflex tearing.

The lubrication-type problem can be characterized as being of the form $h_t + (h^n h_{xxx})_x = 0$; fluid mechanics problems have $n = 3$, typically, but may have additional terms and equations. The main difficulties for numerical solution appear to be related to having these terms present, generally speaking. Numerical methods in previous one spatial dimension studies for problems closely related to this form have used a method of lines approach with differences in choice of spatial approximations and time integration. Some combinations include finite difference spatial approximations on uniformly spaced grids in space with BDF-type solvers in time (e.g., Jensen & Grotberg (1993); Braun & Fitt (2003)); the package PDECOL (Madsen & Sincovec, 1979) which implements finite element discretization in space (Yeo *et al.*, 2003); spectral spatial approximations on a fixed domain with BDF-type solvers in time Haley & Miksis (1991); a dynamically adaptive finite difference method specifically designed to minimize roundoff error with a two-level time stepping scheme (Bertozzi *et al.*, 1994); and a positivity preserving spatial approximation based on a modified PDE that uses finite differences and requires much less resolution than the original PDE (Zhornitskaya & Bertozzi, 2000). A mapped spectral discretization coupled with BDF-type solvers in time was used by Heryudono *et al.* (2008) for a closely related problem with moving ends, specifically the tear film evolution over repeated blink cycles.

The calculations were carried out in this paper with an overset grid method. In an overset grid method, a partial differential equation is discretized and solved on a composite or overlapping grid developed to handle complex geometries or localized solution features. A composite grid contains multiple structured component grids, each being topologically rectangular, with interpolation information used for communication between the separate grids. Composite grids have a number of advantages including: simple grid generation since each component grid is built separately; easy addition or subtraction of bodies or features; and the ability to locally adapt the grid. These appealing features along with the handling of complex geometries will be of importance when considering tear film flow on the entire anterior surface of the eye. They were first used by Volkov (1966, 1968) to solve Poisson's equation on regions with corners (finite domains with piecewise smooth

boundaries) and in principle they utilize the same differencing techniques needed on a Cartesian grid with slight generalization. Code developments in composite grid generation include CMPGRD tools by Chesshire & Henshaw (1990), which later became the OVERTURE framework (Henshaw, 2002); an approach called Chimera grids by Steger and associates was developed independently at NASA (Steger & Benek, 1987). Composite grids have been used successfully for numerical simulations including non-Newtonian Hele-Shaw flow (Fast & Shelley, 2004). Our discretization is finite difference based and again leads us toward our destination of simulations on a two-dimensional eye-shaped domain. Previous work in two dimensions for lubrication type problems has often used ADI methods for spatial approximations on rectangular domains (e.g., Witelski & Bowen (2003) and references therein) but others have used positivity preserving schemes (Diez & Kondic, 2002) and spectral methods (Ye & Change, 1999) for spatial approximations. For finding the thin film flow given by our particular equations on a moving eye-shaped domain, we believe that the overset grid methods as implemented in OVERTURE will be quite effective, and so we start toward that goal by using overset grids in this paper.

After formulating the tear film problem in Section 2, we explore the consequences of three different discretizations of a simplified test problem in Section 3 settling on the most accurate and robust method of the three. Relevant grid parameters for the numerical method are determined from the test problem and subsequently used on the tear film problem. Results for the tear film model are presented in Section 4 with conclusions about the numerical method and reflex tearing follow.

2 Formulation

First, we present the model for the blink cycle of the human tear film derived from lubrication theory.

2.1 Tear film model

A sketch of the tear film model is shown in Figure 2. Primed variables indicate dimensional quantities. The corneal surface is modeled as a flat wall ($y' = 0$) due to the tear film thickness being so much smaller than the radius of curvature of the eye surface (see Berger & Corrsin (1974)). Gravity acts in the positive x'-direction along the wall with the free surface depth $y' = h'(x', t')$ being measured perpendicular to the wall. The velocity components of the film are denoted by (u', v'). The lower lid is fixed at $x' = L'$ while the upper lid moves according to $x' = X'(t')$ with the eye fully open when the upper lid location is $x' = -L'$.

We begin with the Navier-Stokes equation and scale by the half width of the palpebral fissure (corneal surface between the two lids), $L' = 5$mm, in the x'-direction; the characteristic tear film thickness away from the lids $d' = 5\mu$m applied in the y'-direction; the velocity scale, $U_m = 10 - 30$cm/s where U_m is a representative maximum blink closing speed (Doane, 1980; Berke & Mueller, 1998), applied along the tear film; the time scale for real blink speed L'/U_m; and the viscous scale $\mu U_m/(d'\epsilon)$ applied to the pressure p. The small parameter for lubrication theory is the ratio of the length scales, $\epsilon = d'/L'$, approximately 10^{-3}. Other relevant quantities needed in the derivation are the surface tension $\sigma_0 = 45$mN/m (where subscript 0 denotes evaluation at the reference point corresponding to the eye fully open with the lowest average surface concentration of surfactant); the density $\rho = 10^3$kg/m^3; the viscosity $\mu = 10^{-3}$Pa·s; and the gravitational acceleration $g = 9.81$m/s^2.

After nondimensionalization, the leading order terms in the mass conservation equation and momentum conservation equation in the x and y directions, respectively, govern the following parallel flow on $0 \le y \le h(x, t)$:

$$u_x + v_y = 0, \; u_{yy} - p_x + G = 0, \text{ and } p_y = 0. \tag{1}$$

Here $G = \frac{\rho g (d')^2}{\mu U_m}$ is the Stokes number and under typical blink conditions, $G \approx 2.5 \times 10^{-3}$. At the impermeable wall we have the Navier slip condition (to imitate the effects of the mucus and

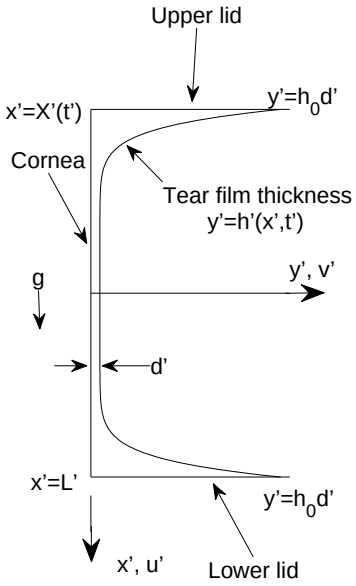

Figure 2: Coordinate system for tear film evolution model. The upper lid moves according to $x' = X'(t')$ while the bottom lid is fixed at $x' = L'$.

microplicae at the corneal surface) and impermeability:

$$u = \beta u_y \text{ and } v = 0, \text{ at } y = 0, \tag{2}$$

where $\beta = L_s'/d'$ and L_s' is the slip length. Using the estimate in Braun & Fitt (2003), the range of β is $10^{-3} \leq \beta \leq 10^{-2}$. At the free surface $y = h(x,t)$ are the kinematic and normal stress conditions, respectively,

$$h_t + uh_x = v - E \text{ and } p = -Sh_{xx}, \tag{3}$$

with $E = \frac{J'}{U_m \epsilon \rho}$ and $S = \frac{\epsilon^3}{\mathrm{Ca}} = \frac{\epsilon^3 \sigma_0}{\mu U_m}$. Here J' is the evaporation mass flux leaving the surface of the film is measured at $J' = 3 \times 10^{-5}$kg m^{-2}s^{-1} by Mathers (1993). For the lowest maximum speed, $S \approx 5 \times 10^{-7}$ and $E \approx 3 \times 10^{-4}$. As for the tangential stress condition, in this paper, we consider the uniform stretching limit where the insoluble surfactant has a very strong Marangoni effect; this causes the surface to behave as though it is uniformly stretched when the upper lid moves or tangentially immobile when the lids are stationary. Mathematically, the surface velocity is given

by

$$u^{(s)} = X_t \frac{1-x}{1-X}; \tag{4}$$

for a derivation, see Braun & King-Smith (2007) or Heryudono *et al.* (2008). Thus, the Marangoni effect determines the tangential motion at leading order; we discuss retaining the capillary term Sh_{xx} at the end of this section. Using the kinematic condition and mass conservation, the free surface evolution equation defined on the domain $X(t) < x < 1$ can be written as

$$h_t + q_x = -E, \tag{5}$$

where

$$q = \int_0^h u(x, y, t)\ dy \tag{6}$$

is the flux of fluid across any cross-section of the film. In particular, the flux function $q(x,t)$,

$$q(x,t) = \frac{h^3}{12}\left(1 + \frac{3\beta}{h+\beta}\right)(Sh_{xxx} + G) + X_t \frac{1-x}{1-X}\frac{h}{2}\left(1 + \frac{\beta}{h+\beta}\right), \tag{7}$$

is obtained from the approximate velocity component u and the uniform stretching limit characterizing the surface velocity of the film.

The upper lid motion, needed to describe the moving domain for tear film evolution equation, is derived from relations found by Berke & Mueller (1998), with modification for partial blinks after Braun and coworkers (Braun & King-Smith, 2007; Heryudono *et al.*, 2008). The parameter λ represents the fraction of the fully open domain (corneal surface) that is exposed when the domain is at its smallest (lids closest together). Therefore, the range of the upper lid is $-1 \le X(t) \le (-2\lambda{+}1)$. The lid motion begins in the closed position with the nondimensional duration of the upstroke $\Delta t_{co} = 3.52$ (0.1758s) followed by the interblink period $\Delta t_o = 500 - 3000$ (25-150s).

$$X(t) = \begin{cases} 1 - 2\lambda - 2(1-\lambda)\left(\frac{t}{\Delta t_{co}}\right)^2 \exp\left[1 - \left(\frac{t}{\Delta t_{co}}\right)^2\right], & 0 \le t \le \Delta t_{co} \\ -1, & t \ge \Delta t_{co} \end{cases}. \tag{8}$$

For the tear film model in this paper, the downstroke (closing phase) will not be used, as we are

studying only the upstroke and interblink periods of the blink cycle. In particular, the focus of reflex tearing study is on the dynamics of the tear film during the interblink period. Jones *et al.* (2005) noted the presence of meniscus-induced thinning at the end of the opening period or the upstroke. They also found that some initial conditions gave reasonable approximations to the film evolution at long times; however, we choose in this work to make use of the ability to generate the film from the lid upstroke.

At the boundaries, we chose to specify the tear film thickness h_0 as well as the value of the flux into the domain at the upper and lower lid. To summarize, the model for the evolution of the tear film thickness is

$$h_t + \left[\frac{h^3}{12}\left(1+\frac{3\beta}{h+\beta}\right)(Sh_{xxx}+G) + X_t\frac{1-x}{1-X}\frac{h}{2}\left(1+\frac{\beta}{h+\beta}\right)\right]_x = -E, \tag{9}$$

on the moving domain $X(t) < x < 1$ with boundary conditions

$$h(X(t),t) = h_0, \quad h(1,t) = h_0, \tag{10}$$

$$q(X(t),t) = X_t h_0 + Q_{top}, \quad q(1,t) = Q_{bot}, \tag{11}$$

and initial condition

$$h(x,0) = H_{min} + (h_0 - H_{min})\left[\frac{\lambda-1}{\lambda} + \frac{x}{\lambda}\right]^m. \tag{12}$$

Detailed initial conditions are given in section 2.2 and detailed boundary fluxes are given in section 2.3. A summary of all the parameters introduced in the formulation of the tear film model is given in Table 1.

We note that we have kept the surface tension term involving Sh_{xx} in the normal stress condition despite the small numerical value of S. We have done so in order to approximate the meniscus region of the film which requires specifying both h and the flux of fluid q at the boundary. The relatively slow movement of the meniscus region in typical tear film observations justify this approach with regard to experimental comparison (e.g., Johnson & Murphy (2006)). We are not aware of how to achieve this level of modeling for this problem without retaining this surface tension term.

Evolution Equation and Boundary Conditions, (5) & (7):		
Parameter	Description	Value
σ_0	Surface tension	45mN/m
ρ	Density	10^3kg/m^3
μ	Viscosity	10^{-3}Pa.s
U_m	Velocity scale	10cm/s
E	Constant evaporation rate	3.0×10^{-4}
S	Inverse capillary number	5.0×10^{-7}
β	Slip length	10^{-3}
G	Stokes number	2.5×10^{-3}

Upper Lid Motion, (8):		
Parameter	Description	Value
Δt_{co}	Duration of upstroke	3.52
Δt_o	Duration of interblink	3000
λ	Fraction of fully open eye domain	0.1

Table 1: Values along with description of the parameters introduced in tear film model formulation. Unless otherwise stated, these values were used in all simulations discussed in Section 4. All parameters below U_m are dimensionless.

2.2 Domain mapping and initial conditions

To conveniently discretize the changing domain length in the tear film equation, we chose to transform the moving domain $X(t) \leq x \leq 1$ into the fixed domain $-1 \leq \xi \leq 1$ with the mapping

$$\xi = 1 - 2\frac{1-x}{1-X(t)}. \tag{13}$$

The change of variables $h(x,t) = H(\xi(t),t)$ gives the following relationships for the derivatives in the partial differential equations

$$h_t = H_t - H_\xi X_t \frac{1-\xi}{1-X}, \quad h_x = H_\xi \frac{2}{1-X}, \quad h_{xx} = H_{\xi\xi}\left(\frac{2}{1-X}\right)^2, \quad \text{etc.} \tag{14}$$

Given the mapped parameters, it is now easier to describe the initial condition of the tear film problem. We use the polynomial

$$H(\xi,0) = H_{min} + (h_0 - H_{min})\xi^m, \tag{15}$$

where H_{min} is found by integrating the polynomial over $-1 \leq \xi \leq 1$ and equating to a specified area (representing the tear film volume). The parameter m is an even integer ranging from 2 to 16, but typically used $m = 4$.

2.3 Flux functions for reflex tearing

Flux conditions are specified at the boundaries to approximate the drainage flow along with tear supply along the lid margins. In particular, the conditions are

$$q(X(t), t) = X_t h_0 + Q_{top} \text{ and } q(1, t) = Q_{bot} \tag{16}$$

where Q_{top} and Q_{bot} are the respective fluxes into the domain at the upper and lower lids. The functions we use for Q_{top} and Q_{bot} are variants of functions proposed by Jones *et al.* (2005) and Heryudono *et al.* (2008). Jones *et al.* (2005) assumed there is a certain flux from under the upper eyelid and therefore developed the following flux functions, which we designate FPLM for *flux proportional to lid motion*,

$$Q_{top} = -X_t h_e \text{ and } Q_{bot} = 0. \tag{17}$$

The parameter h_e represents the proportion of the tear film thickness being exposed as the upper lid opens. Using the estimates from Heryudono *et al.* (2008), we chose $h_e = 0.6$. Building upon the FPLM boundary conditions of Jones *et al.* (2005), Heryudono *et al.* (2008) included Gaussian functions to model both the drainage through the puncta and the influx of tear fluid from the lacrimal gland. The detailed equations for flux functions are of the form

$$Q^+_{top} = -X_t h_e - 2 f_{out} Q_{0p} \exp\left[-\left(\frac{t - t_{out}}{\Delta t_p}\right)^2\right] + f_{top} Q_{0lg} \exp\left[-\left(\frac{t - t_{in}}{\Delta t_{co}/2}\right)^2\right] \tag{18}$$

for the top lid and

$$Q^+_{bot} = -2(1 - f_{out}) Q_{0p} \exp\left[-\left(\frac{t - t_{out}}{\Delta t_p}\right)^2\right] + (1 - f_{top}) Q_{0lg} \exp\left[-\left(\frac{t - t_{in}}{\Delta t_{co}/2}\right)^2\right] \tag{19}$$

for the bottom (see Figure 3). The influx from the lacrimal gland is modeled by the terms proportional to Q_{0lg} while terms proportional to Q_{0p} represent the drainage through the puncta in the lacrimal drainage system developed by Doane. The heights of the Gaussian peaks, Q_{0lg} and Q_{0p}, were chosen so that the average value of the Gaussians over a blink cycle is 1.2μl/min, which is the estimated steady supply from the lacrimal gland (Mishima *et al.*, 1966). Thus, the average drainage flux from the puncta matches the average lacrimal gland supply over a blink cycle. The influxes from the lacrimal gland and punctal drainage are distributed between the top and bottom lid by parameters f_{top} and f_{out}, respectively. Heryudono *et al.* (2008) referred to these boundary conditions as FPLM+.

The new variant includes reflex tearing, which is aqueous fluid supplied to the tear film from the lacrimal gland due to external or internal stimuli. Here we model the influx of reflex tears using the FPLM+ boundary conditions with the addition of a pulse composed of two hyperbolic tangent functions. The functions, shown in Figure 3, are of the form

$$Q_{top} = Q_{top}^{+} + g_{top} Q_{0r} \left[\frac{\tanh\left(\frac{t-t_{ron}}{\Delta t_{ron}}\right)}{2} - \frac{\tanh\left(\frac{t-t_{ron}-t_{roff}}{\Delta t_{roff}}\right)}{2} \right] \tag{20}$$

and

$$Q_{bot} = Q_{bot}^{+} + (1-g_{top}) Q_{0r} \left[\frac{\tanh\left(\frac{t-t_{ron}}{\Delta t_{ron}}\right)}{2} - \frac{\tanh\left(\frac{t-t_{ron}-t_{roff}}{\Delta t_{roff}}\right)}{2} \right]. \tag{21}$$

The influx of reflex tears begins around $t = t_{ron}$ and ends at $t = t_{ron} + t_{roff}$ with nondimensional flux $Q_{0r} = \gamma Q_{mT}$, where Q_{mT} is the nondimensional flux of the estimated steady supply from the lacrimal gland of 1.2μl/min. Here the stimulus or trigger for the reflex tearing depended only on time elapsed after the blink, which could correspond to corneal dehydration. The parameter γ was chosen to be $2 \leq \gamma \leq 9$, leading to reflex tear flow rates falling in the range of estimates by Farris *et al.* (1981) of $5.71 \pm 5.86\mu$l/min. As in the FPLM+ boundary conditions, the influx associated with reflex tearing was interpolated between the upper and lower lid by the parameter g_{top}. This is possible physiologically because upper and lower menisci are connected through the canthi (Maurice, 1973).

Flux Functions, (20) & (21):		
Parameter	Description	Value
h_e	Thickness of film from under upper lid	0.6
Q_{mT}	Estimated steady supply from lacrimal gland	0.01
Q_{0p}	Height of punctal drainage Gaussian peak	0.0297
Q_{0lg}	Height of lacrimal gland Gaussian peak	0.3371
f_{top}	Fraction of lacrimal gland influx from upper lid	0.65
f_{out}	Fraction of punctal drainage from upper lid	0.60
t_{out}	Location of punctal drainage Gaussian peak	$2\Delta t_p + \Delta t_{co}$
t_{in}	Location of lacrimal gland Gaussian peak	Δt_{co}
Δt_p	Width of punctal drainage Gaussian	10
Q_{0r}	Height of reflex tearing pulse	$4Q_{mT}$
g_{top}	Fraction of reflex tearing influx from upper lid	0.80
t_{ron}	Time when reflex tearing pulse starts	$\Delta t_{co} + 150$
t_{roff}	Duration of time reflex tearing pulse is on	50
Δt_{ron}	Width of the on-ramp of the reflex tearing pulse	1/2
Δt_{roff}	Width of the off-ramp of the reflex tearing pulse	1

Table 2: Values along with description of the nondimensional parameters introduced in reflex tearing flux functions. Unless otherwise stated, these values were used in all simulations discussed in Section 4.

3 Numerical methods

Three different numerical approaches, referred to as the ODE, DAE and reformulated ODE (RODE) approaches, were investigated on a simplified nonlinear test problem. All three numerical methods used the method of lines coupled with finite differences, but they differed in the enforcement of the flux boundary conditions. In the method of lines, spatial derivatives are first discretized with time remaining continuous. Then an appropriate time discretization is used on the resulting system of ordinary differential equations (ODEs) for the grid points. In all time integration calculations, both ODEs and differential-algebraic equations (DAEs), we used `ode15s` in MATLAB (Shampine *et al.*, 1999) which is suitable for stiff ODEs.

The numerical simulations are computed on a composite grid which contains multiple component grids that cover the domain and overlap where they meet. Each point in the composite grid is designated as one of three types: interpolation, discretization or unused. Discretization points are where the partial differential equation and boundary conditions are approximated, while in-

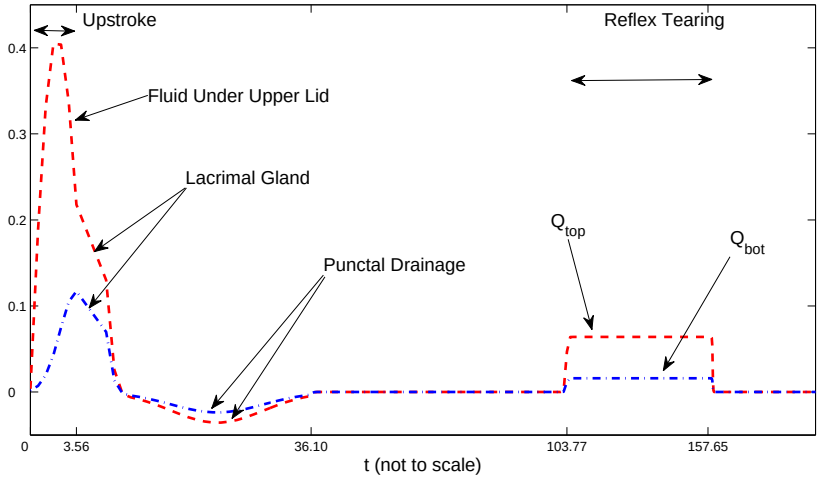

Figure 3: An example of reflex boundary fluxes Q_{top} and Q_{bot} with $\lambda = 0.1$.

terpolation points provide communication between the different component grids. The solution is found at a interpolation point by the evaluation of an interpolant built from the solution on the corresponding overlapping grid. Grid points that are neither interpolation nor discretization points are considered unused grid points.

An example of a typical composite grid we used in the tear film calculation is shown in Figure 4. There is a total of three component grids with grid points denoted by ξ_j^k for $k = 1, \ldots, 3$ and $j = 0, \ldots, N_k$. The two fine boundary grids ξ^1 and ξ^3 captured the rapid changes in tear film thickness $H(\xi, t)$ around the menisci while the coarse grid ξ^2 covered the remaining part of the domain. Solution values at the grid points are denoted by $H(\xi_j^k, t) = H_j^k(t)$. Two interpolation points are needed on each component grid at each overlap since the finite differences require the function values of at most two neighboring points. We applied explicit interpolation in all calculations, meaning enough overlap is provided to avoid the coupling of interpolation points on different component grids. All interpolation is performed using Lagrange polynomials where the Lagrange basis polynomials are evaluated using barycentric weights (Berrut & Trefethen, 2004). The barycentric formula exploits a symmetry which minimizes rounding errors.

To avoid the drastic disparity in grid spacing that can occur in a composite grid containing a fine grid overlapping a coarse grid as in Figure 4, a grid stretch function was developed to elongate the spacing of the fine grid to match the spacing of the coarse grid in the overlap region. It is inefficient

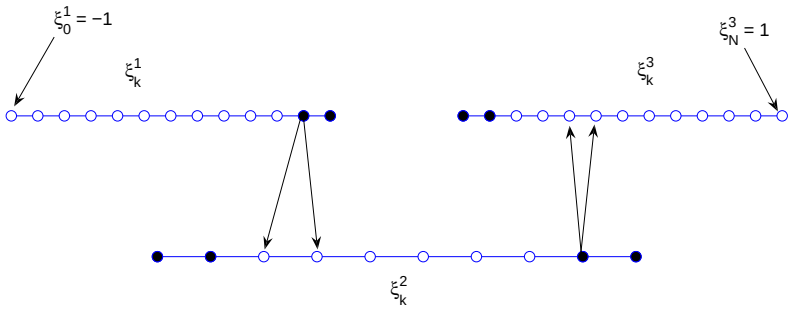

Figure 4: A one-dimensional composite grid with discretization points (open circles) and interpolation points (closed).

to have a fine grid overlapping a coarse grid since the solution must be smoothly represented on each grid and thus fine grid points are wasted. The clustering or separating of grid lines is often a main feature in many software packages that manipulate and create composite or overset grids including Overture (Henshaw, 2002; Chesshire & Henshaw, 1990). The details of the stretching are given in Appendix A.

Another aspect of the computation investigated was the conservation of volume. The error in volume conservation is chosen for the nonlinear tear film model as an indicator of the accuracy of numerical schemes since no exact solution is available. For a particular value of time, the volume is defined to be

$$V(t) = \int_{X(t)}^{1} h(x,t)dx = \frac{1 - X(t)}{2} \int_{-1}^{1} H(\xi,t)d\xi. \tag{22}$$

The details of computing this error can be found in Appendix A as well. Next, we formulate a simplified nonlinear test problem and then explain the three different numerical approaches in detail.

3.1 Test problem

In the simplified nonlinear test problem, we create a partial differential equation of the form (5) with a space- and time-dependent forcing term so that the exact solution is

$$h(x,t) = (h_0 - 1)e^{-[x-X(t)]/x_0} + 1.$$

Here

$$X(t) = (1-\lambda)\cos(t) - \lambda \tag{23}$$

for $0 \leq t \leq 2\pi$ is the prescribed periodic motion of the upper lid corresponding to a sinusoidal complete blink cycle first studied by Braun (2006) and Braun & King-Smith (2007) (see Figure 2 for coordinate system used). Note that the blink cycle for the test problem includes the downstroke or the closing of the lids, which is again excluded in the reflex tearing study of the tear film to follow. The exact solution plotted in Figure 5 mimics features seen in the human tear film at the upper lid such as the meniscus and rapid decay to unity (intended to mimic the characteristic tear film thickness). We study fourth-order partial differential equations of the form

$$h_t + q_x = g(x,t) \tag{24}$$

(which only departs from the tear film equation by the nonconstant forcing function $g(x,t)$) and with flux function

$$q(x,t) = \frac{h^3}{12} S h_{xxx}. \tag{25}$$

The boundary conditions are

$$h(X(t),t) = h_0, \tag{26}$$

$$h(1,t) = (h_0 - 1)e^{-[1-X(t)]/x_0} + 1, \tag{27}$$

and

$$q(X(t),t) = \frac{h_0^3}{12} S \frac{1-h_0}{x_0^3}, \tag{28}$$

$$q(1,t) = \frac{\left[(h_0-1)e^{-[1-X(t)]/x_0}+1\right]^3}{12} S \frac{1-h_0}{x_0^3} e^{-[1-X(t)]/x_0}. \tag{29}$$

Specifying the flux at the boundary boils down to specifying the third derivative of the thickness h_{xxx}. The forcing function associated with the nonlinear test problem is

$$\begin{aligned} g(x,t) &= \frac{X_t(t)(h_0-1)}{x_0} e^{-[x-X(t)]/x_0} \\ &+ \frac{[(h_0-1)e^{-[x-X(t)]/x_0}+1]^2}{4} \frac{1-h_0}{x_0} e^{-[x-X(t)]/x_0} S \frac{1-h_0}{x_0^3} e^{-[x-X(t)]/x_0} \\ &+ \frac{[(h_0-1)e^{-[x-X(t)]/x_0}+1]^3}{12} S \frac{(h_0-1)}{x_0^4} e^{-[x-X(t)]/x_0}. \end{aligned} \tag{30}$$

Next we explain the three numerical methods used to solve the nonlinear test problem and subsequently the reflex tearing calculations. In the next three sections, we use the nonlinear test problem to describe the three algorithms in detail.

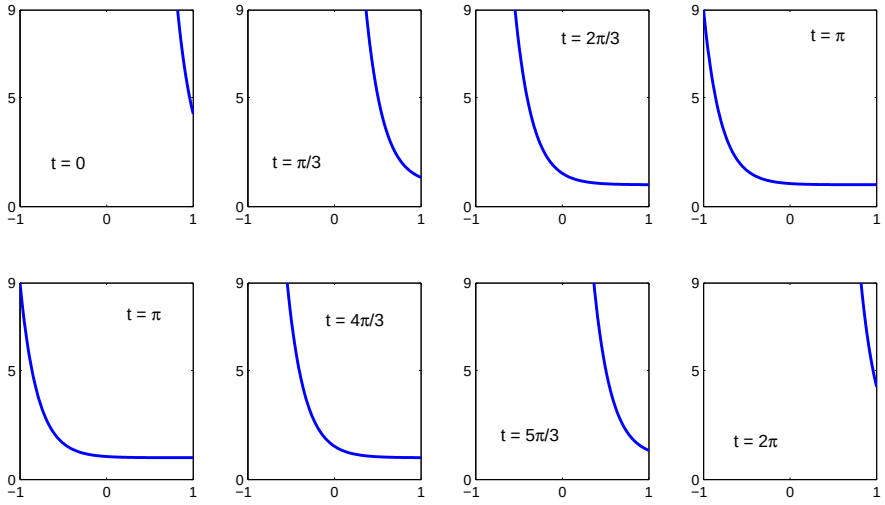

Figure 5: Plot of the exact solution $h(x,t)$ to the nonlinear simplified test problem over one blink cycle for different values of t with $h_0 = 9$, $x_0 = 0.2$ and $\lambda = 0.09$.

3.2 ODE approach

In the direct ODE approach the flux boundary conditions are enforced through the introduction of fictitious points and direct manipulation of the variable H. The transformed nonlinear test problem is

$$H_t - \frac{X_t(1-\xi)}{1-X}H_\xi + \left(\frac{2}{1-X}\right)\left[\frac{H^3}{12}S\left(\frac{2}{1-X}\right)^3 H_{\xi\xi\xi}\right]_\xi = G(\xi,t), \tag{31}$$

$$H(-1,t) = h_0, \quad H(1,t) = (h_0-1)e^{-[1-X(t)]/x_0} + 1, \tag{32}$$

$$H_{\xi\xi\xi}(-1,t) = -\left(\frac{1-X(t)}{2}\right)^3 \frac{(h_0-1)}{x_0^3}, \tag{33}$$

$$H_{\xi\xi\xi}(1,t) = -\left(\frac{1-X(t)}{2}\right)^3 \frac{(h_0-1)}{x_0^3} e^{-[1-X(t)]/x_0}, \tag{34}$$

where $G(\xi,t)$ is the mapped version of $g(x,t)$. The Dirichlet boundary conditions are imposed simply by setting $H_0^1(t) = h_0$ and $H_N^3(t) = (h_0-1)e^{-(1-X)/x_0} + 1$. Satisfying the remaining flux boundary condition requires more effort. Second-order accurate finite differences are used to approximate H_ξ, $H_{\xi\xi\xi}$ and $H_{\xi\xi\xi\xi}$. Using a centered difference to estimate $H_{\xi\xi\xi\xi}(\xi_1^1,t)$ and $H_{\xi\xi\xi}(\xi_1^1)$ requires the addition of the fictitious point ξ_{-1}^1. The function value $H(\xi_{-1}^1,t) = H_{-1}^1(t)$ is found by requiring that the local interpolant, which passes through $(\xi_{-1}^1, H_{-1}^1(t)), .., (\xi_3^1, H_3^1(t))$, to satisfy the boundary condition (33). This leads to a second-order accurate expression for $H_{-1}^1(t)$ in terms of $H_0^1(t), ..., H_3^1(t)$ and $H_{\xi\xi\xi}(-1,t)$. A similar approach is used in the approximation of $H_{\xi\xi\xi\xi}(\xi_{N-1}^3,t)$ which requires the fictitious point ξ_{N+1}^3. In this approach, we then solve the system of ODEs for $H_j^k(t)$ at the interior grid points.

3.3 DAE approach

The DAE approach eliminates the need for an approximation of the flux boundary condition by rewriting the partial differential equation as a semiexplicit DAE of index one with the flux as a new dependent variable $Q(\xi,t)$. The DAE system for the nonlinear test problem with Dirichlet

boundary conditions is

$$H_t - \frac{X_t(1-\xi)}{1-X}H_\xi + \left(\frac{2}{1-X}\right)Q_\xi = G(\xi,t) \tag{35}$$

$$0 = \frac{H^3}{12}S\left(\frac{2}{1-X}\right)^3 H_{\xi\xi\xi} - Q \tag{36}$$

$$H(-1,t) = h_0,\ H(1,t) = (h_0-1)e^{-[1-X(t)]/x_0} + 1, \tag{37}$$

$$Q(-1,t) = \frac{h_0^3}{12}S\frac{(1-h_0)}{x_0^3}, \tag{38}$$

$$Q(1,t) = \frac{[(h_0-1)e^{-[1-X(t)]/x_0^3}+1]^3}{12}S\frac{(1-h_0)}{x_0}e^{-[1-X(t)]/x_0}, \tag{39}$$

where $G(\xi,t)$ is defined above. Second-order accurate finite differences are used to approximate Q_ξ, H_ξ and $H_{\xi\xi\xi}$. For the fluxes at grid points, we define $Q(\xi_j^k,t) = Q_j^k(t)$. Dirichlet boundary conditions are enforced by setting the values of $H_0^1(t)$, $H_N^3(t)$, $Q_0^1(t)$ and $Q_N^3(t)$ from the given boundary values. In this approach, we solve the resulting DAE system for $H_j^k(t)$ and $Q_j^k(t)$ on the interior grid points.

3.4 RODE approach

Here we take an "ODE approach" discussed in Shampine *et al.* (1999) when solving a DAE of index one where standard ODE solvers are implemented with the following variant. When the integrator needs to evaluate the right-hand side of (35), it first solves the algebraic equation (36) for $Q(\xi,t)$ and the answer is substituted into (35) resulting in an ODE system. Thus, the flux is computed as an intermediate step with its own interpolant; the flux is then differenced to update H. As for the enforcement of the boundary conditions, at the grid point ξ_1^1, we used the discretization (note, $\Delta\xi^1 = \xi_1^1 - \xi_0^1$):

$$\frac{dH_1^1(t)}{dt} = \left(\frac{X_t(1-\xi_1^1)}{1-X}\right)\frac{H_2^1(t) - H(-1,t)}{2\Delta\xi^1} - \left(\frac{2}{1-X}\right)\frac{Q_2^1(t) - Q(-1,t)}{2\Delta\xi^1}, \tag{40}$$

where

$$Q_2^1(t) = \frac{\left[H_1^1(t)\right]^3}{12}S\left(\frac{2}{1-X}\right)^3\frac{-0.5H(-1,t) + H_1^1(t) - H_3^1(t) + 0.5H_4^1(t)}{(\Delta\xi^1)^3} \tag{41}$$

is the second-order finite difference approximation to $Q(\xi_2^1, t)$ found using the Dirichlet boundary condition $H(-1, t) = h_0$. Thus, we solve the resulting ODE system for $H_j^k(t)$ on the interior grid points. Note that we apply the exact flux from the boundary condition at the endpoints of the domain rather than computing a difference approximation of Q found from fictitious points. This seemingly small change of algorithm has detectable effects on the accuracy and stability of the scheme.

3.5 Test problem results

We chose the exact solution parameters to be $h_0 = 9$, $x_0 = 0.2$ and $\lambda = 0.09$ as in Figure 5 along with $S = 4 \times 10^{-5}$, unless otherwise stated. The composite grid used in the following calculations differs from the tear film grid shown in Figure 4 by having two component grids, that is ξ^1 and ξ^2. The difference is due to the exact solution having only one meniscus located at the moving end (Figure 5) rather than a meniscus at each end as in the tear film. Each component grid has uniform spacing with $\Delta\xi = \Delta\xi^1 \approx \Delta\xi^2$ and overlapping at $\xi = 0$.

We found the ODE approach was not able to compete with the DAE and RODE methods in the calculation of the nonlinear test problem. The ODE code could only execute in a comparable time to the DAE and RODE method on composite grids containing fewer than 300 grid points. Numerical investigation reveals the approximation of the fourth derivative and therefore q_x suffers from roundoff error. Figure 6 displays the absolute error in the approximation of q_x on a composite grid containing 1000 points. The large error terms are confined to one grid point in the RODE method, while in the ODE method the large error terms extend a quarter of the way into the computational domain.

In comparing the DAE approach to the RODE approach, we found the latter to be more robust. In particular, the RODE code executed faster than the DAE code and calculated solutions at least as accurately. Here accuracy is measured by the maximum absolute error of $H(\xi, t)$ for a particular value of time. Figure 7 compares the maximum absolute error of the two different methods on a composite grid containing 1000 grid points over one cycle of end motion given by Equation 23. Based upon these findings, the RODE approach was used for all subsequent computations.

A few more findings regarding the RODE approach are relevant here. Figure 8 plots the

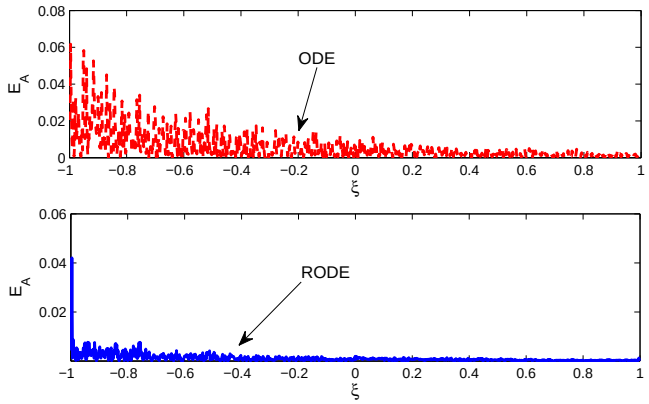

Figure 6: The absolute error in the spatial approximation of $q_x = [2/(1-X)]Q_\xi$ at $t = 0.01$ on a composite grid containing 1000 points by the ODE and RODE method. The maximum in both plots occurs at the left boundary with value 0.0616 in the ODE method and value 0.0420 in the RODE approach.

maximum absolute error (solid line) at $t = 4.06$ as a function of the mesh size ($\Delta\xi$). The figure also shows how a least-squares fit of the form $c(\Delta\xi)^\alpha$ (dashed line) gives the convergence order $\alpha = 2.28$. This is strong numerical evidence for second order accuracy. As for the reliability of the error in volume conservation as a diagnostic tool, we found it to be a rough indicator of (but not a bound on) the maximum relative error over a simulation; see Appendix A for more details. It is interesting to note that the size of the parameter S affects the performance of the RODE method due to error terms from the spatial approximation of the form $S(H_j^k)^3(\Delta\xi)^2$, where H_j^k can be as large as $h_0 = 9.0$. Thus, the nonlinear test problem could not be solved with $S = 1$, but it could be reliably solved with $10^{-7} \le S \le 10^{-3}$.

The last item investigated on the test problem was the dependence on the composite grids. Since the exact solution changed less rapidly on the right half of the interval ($0 < \xi < 1$), it is possible to reduce the total number of grid points by using a coarser right-hand grid while still meeting the accuracy requirement for the computed solution. In particular, results for fine spacing $\Delta\xi^1 = 1/1500$ are shown in Table 3. In the stretched coarse/fine grid, the fine left grid is stretched by the function described in the Appendix A. The coarse grid spacing is $\Delta\xi^2 = 6\Delta\xi^1$.

Based on the findings for the nonlinear test problem, we chose a composite grid in tear film calculations with three component grids to capture the rapid changes in each meniscus. One grid spans the left-hand side of the computational domain, typically $[-1, 0]$, with fine spacing

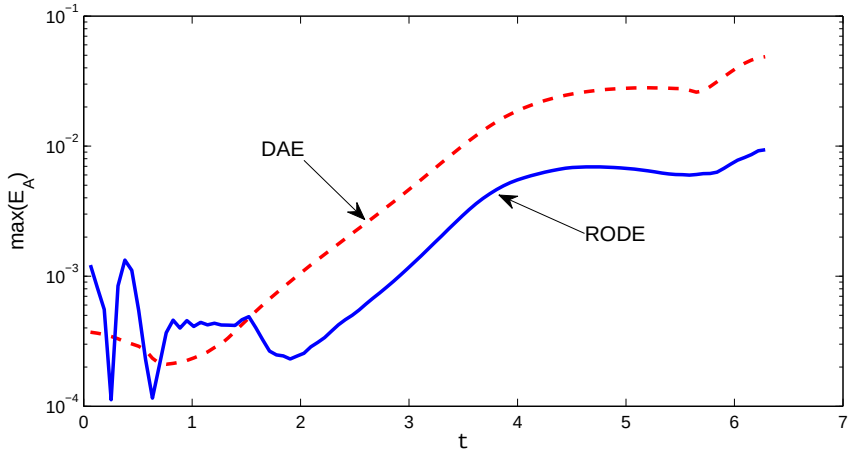

Figure 7: The maximum absolute error of $H(\xi, t)$, E_A, in the nonlinear test problem calculated on a composite grid containing 1000 points over one cycle by the DAE and RODE method.

Grid	Nonlinear Test		
	grid points	$\max(E_V)$	$\max(E_A)$
both uniform	3009	5.42×10^{-4}	3.3×10^{-3}
coarse/fine	1771	1.00×10^{-3}	6.0×10^{-3}
stretched coarse/fine	1668	7.27×10^{-4}	3.2×10^{-3}

Table 3: Comparison of the maximum volume conservation and absolute error over one cycle on different composite grids for the nonlinear test problem.

$\Delta\xi^1 = 1/1501$. The grid is stretched into the coarse center grid usually passing over $[0, 0.3]$ with $\Delta\xi^2 = 5/1500.5$. Finally, the last grid spans the right-hand side of the domain, typically $[0.3, 1]$, with $\Delta\xi^3 = 1/1501$ and is again stretched into the coarse center grid. Figure 9 displays sections of length 0.15 of a typical tear film computational grid on $[-1, 1]$. The comparison of the spacing between grid points in panel 1 to panel 2 of the left stretched fine grid (denoted by circles) illustrates the workings of the stretch function applied to a overlapping grid.

4 Tear film results

We now turn to the solving the tear film evolution equation. Experimental measurements of the effect of reflex tearing have been taken by King-Smith *et al.* (2000) and of particular interest are the results for the six-minute man alluded to in the introduction. The single thickness measurement in

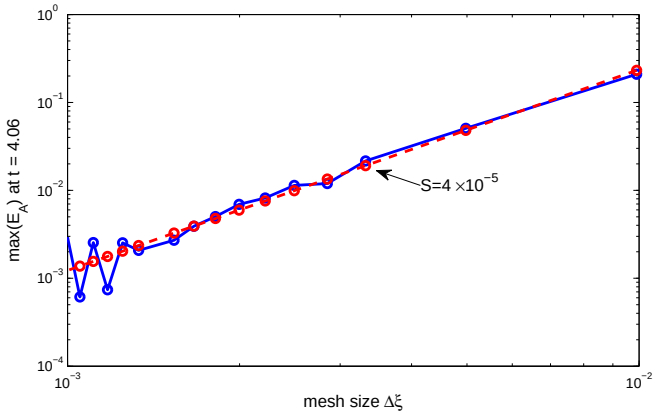

Figure 8: The maximum absolute error (solid) at $t = 4.06$ in the nonlinear test problem along with the least squares fit curves to $\eta(\Delta\xi)^\alpha$, where $\alpha = 2.28$ and $S = 4 \times 10^{-5}$.

the center of the cornea was obtained by measuring reflection spectra at normal incidence. Fourier analysis of the reflectance spectral yielded, among other data, the tear film thickness in a small spot. King-Smith *et al.* (2000) observed that the tear film thinned for the first minute from 3μm to 2μm, then increased to 5μm before decreasing to 2μm (see Figure 14 below). In a different subject, the thickness increased to 9μm, which was the highest measured value observed. King-Smith *et al.* (2000) hypothesized that there was reflex tearing causing excess fluid to travel down the cornea giving relief to the irritation. Our computational results are compared with these findings.

We begin with a computation with the parameter values as in Table 1 and Table 2 with both gravity ($G = 2.5 \times 10^{-3}$) and evaporation ($E = 3.0 \times 10^{-4}$) active. In summary, the upstroke occurs in about 0.18s, followed by an interblink period where the lids remain open for 150s. Reflex tearing begins 7.5s into the interblink period at a rate of 4.8μl/min and ends 2.5s later. In all calculations that follow the parameters above are used unless otherwise stated.

Figure 10 displays the evolution of the film; the left end in the panels corresponds to the upper end (i.e., upper lid) of the tear film. In the top panel, the film is laid down during the upstroke. The next panel shows relaxation, characterized by capillary-driven thinning near the lids, creating what is referred to as black lines in the eye literature (McDonald & Brubaker, 1971; Wong *et al.*, 1996; Creech *et al.*, 1998). In the third panel is the simulation during the influx from reflex tearing for $t_{ron} \le t \le t_{ron} + t_{roff}$. The film is lifted up at the lids as 80% of the constant reflex tears influx enters in through the upper lid and the remaining 20% in through the bottom. The interior slowly

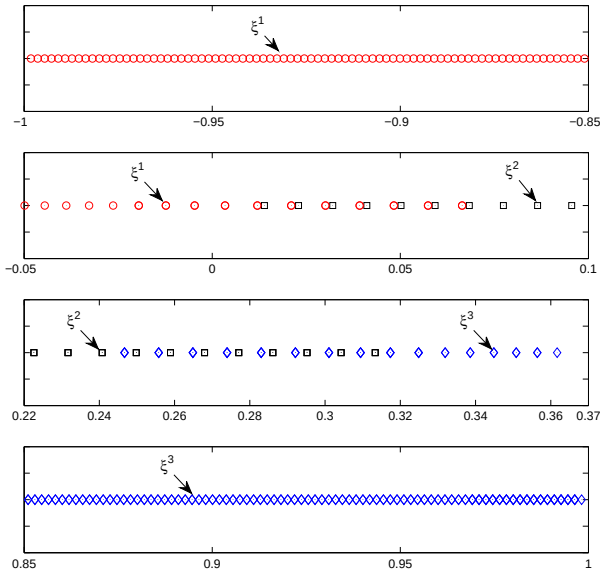

Figure 9: A typical distribution of the grid points on $[-1, 1]$ in a tear film model simulation with each panel showing a section of width 0.15 in the computational domain. Panel 1 (top): Fine grid at left end. Panel 2: Overlap region of the left stretched fine and center coarse grids. Panel 3: Overlap region of the center coarse and right stretched fine grids. Panel 4 (bottom): Fine grid at right end.

thins with the free surface being tangentially immobile. The local thinning regions or black lines cause limited resistance to fluid movement when reflex tearing is turned on. That is, reflex tearing can break through the black line region. The final panel displays the relaxation of the tear film for the remaining time period with no-flux boundary conditions. In the beginning of the relaxation period, gravity drains the upper meniscus causing a bulge of tear fluid to move down the cornea eventually reaching and lifting up the local thinning region at the lower lid. After this bulk of fluid drains from the upper meniscus, and also before and after the lifting of the lower black line, there is again capillary thinning near the ends. Throughout the entire relaxation period the thickness profile is decreased due to evaporation. We note that we currently cannot continue the simulation for a full 360s on account of film breakup at the lower lid.

The film thickness at the center of the cornea as a function of time during the interblink period with different values of g_{top} are shown in Figure 11. The bulge of tear fluid that drains from the upper meniscus (described above as well as illustrated in Figure 10) causes the jump in the thickness

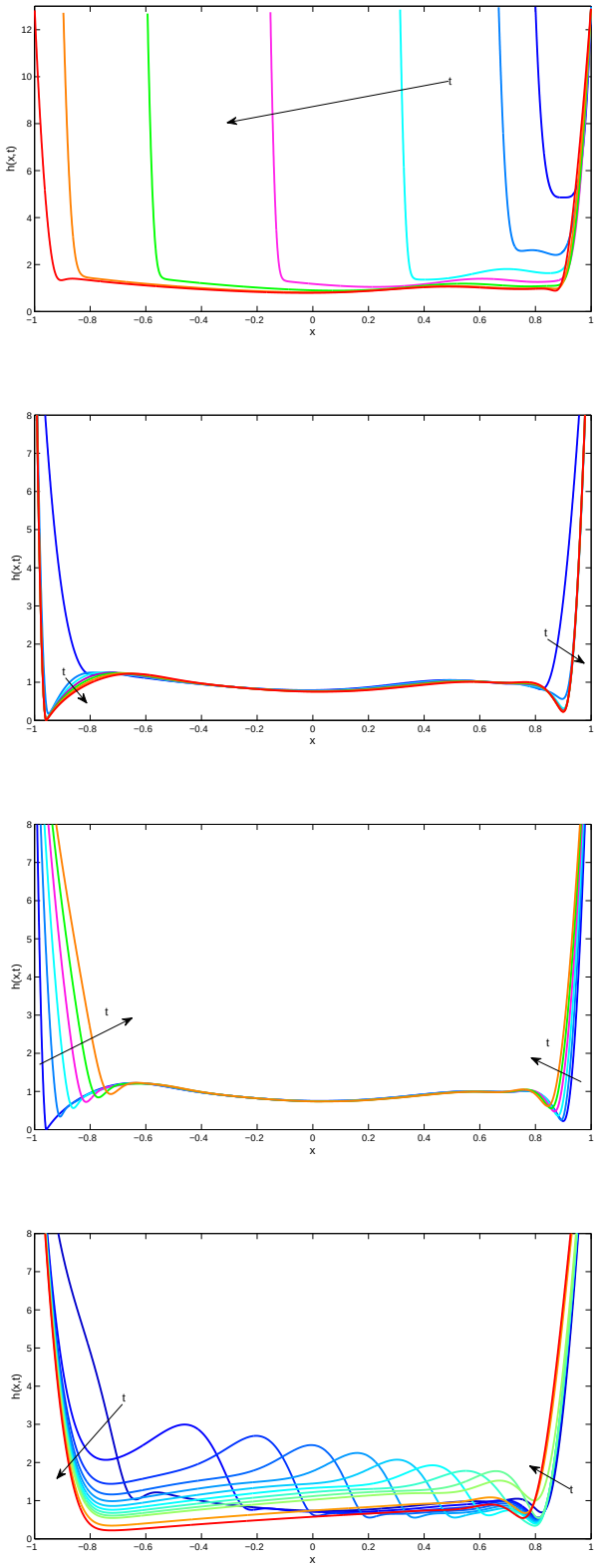

Figure 10: Tear film evolution with gravity and evaporation. Panel 1 (Top): Upstroke of the blink cycle. Panel 2: Relaxation before reflex tearing is turned on. Panel 3: Reflex tearing during $t_{ron} \leq t \leq t_{ron} + t_{roff}$. Panel 4: Relaxation after reflex tearing is turned off, $t_{ron} + t_{roff} \leq t \leq \Delta t_{co} + \Delta t_o$.

profiles. The decrease during the first 10s is credited to evaporation effects since the slope of a fitted linear function for each curve during this time interval is approximately -2.9×10^{-4} (recall $E = 3.0 \times 10^{-4}$). Therefore, gravitational and capillary effects balance in the center of the cornea during this period. For the decrease in profile at later times, the slope of a fitted linear function for each curve from 100s until film breakup ranges from -3.9×10^{-4} to -3.6×10^{-4}. Thus, the center of the cornea is still experiencing a combination of gravitational and capillary effects after the bulge of tear fluid has passed.

We now focus on the evolution of the tear film during and after reflex tearing and its dependence on the parameters by observing the thickness in the middle of the film, $h(0,t)$, and its dependence on g_{top}. By varying g_{top}, we redistribute the influx of tear fluid from reflex tearing between the upper and lower lid and thus vary the amount of fluid in the upper meniscus. In the beginning of the relaxation period after the reflex tearing is turned off (panel 4 of Figure 10), decreasing g_{top} decreases the gravitational effects and also increases the capillarity effects relative to the gravity effects. Therefore, as g_{top} is decreased, there is more resistance to tear fluid draining down the cornea, resulting in the delay and decrease of the peak in the center thickness shown in Figure 11. Furthermore, the size of the peak decreases while the time interval of the jump increases. We also varied the slip coefficient as is shown in Figure 12. Increasing the slip to $\beta = 0.1$ results in an earlier arrival of the peak thickness at the center of the film because the film is more mobile with increased slip. The center thickness decreases at the same rate for either g_{top} value once the transient increase is passed. Results for $\beta = 0$ and 10^{-3} are difficult to distinguish graphically.

It is interesting to note that we can reproduce the center thickness profile with $g_{top} = .50$ by choosing the same parameters except $g_{top} = .80$ and $Q_{0r} = 2.5Q_{mT}$. In both of these cases, the area under the curve Q_{top} during reflex tearing is the same while is the area under Q_{bot} is different. The evolution of the tear film in both cases is shown during relaxation after the reflex tearing has been turned off in Figure 13. The difference in the evolution is confined to the bottom quarter of the cornea. Thus, the center thickness profile is sensitive to only changes in the influx for the upper meniscus.

Figure 14 compares the center thickness from Figure 13, shifted in time to visually align the beginning of the increase in the profile, with the measurement data found by King-Smith *et al.*

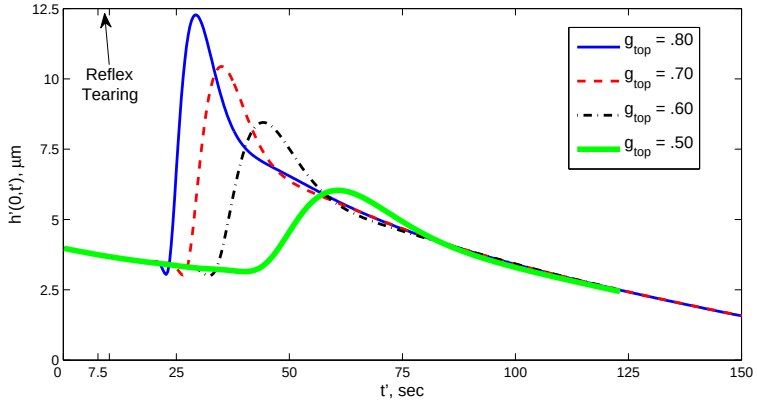

Figure 11: Film thickness at the center of the cornea as a function of time (t') for different values of g_{top}.

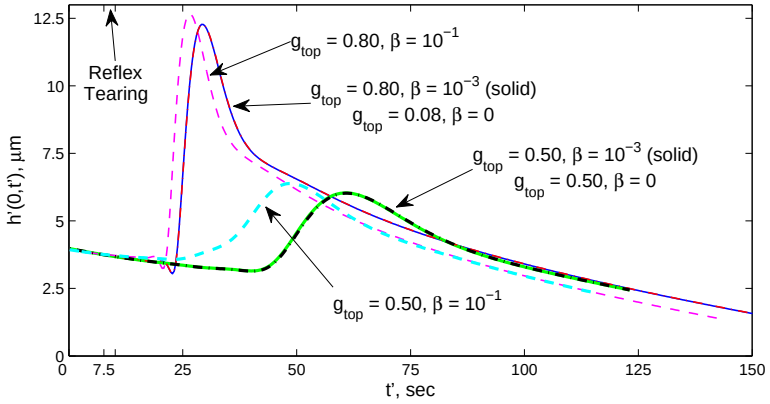

Figure 12: Film thickness at the center of the cornea as a function of time (t') for different values of g_{top} and β.

(2000) and shows qualitative agreement. Our computation can capture the initial decrease identified as an evaporation effect, but we are restricted to turn on reflex tearing early (7.5s) due to tear film breakup at the black lines. We can also capture the peak caused by gravity draining a pulse of tear fluid down the cornea. The increase in tear film thickness is comparable with the measured data having a height increase of 2.8μm over 20.7s. A feature missing in our simulations shown thus far, which occurs in the measured data of King-Smith *et al.* (2000), is the leveling off for later times. In attempt to capture the leveling off, we modified the reflex tearing functions to include an additional constant supply for later times. That is, rather than having the reflex tearing pulse turn completely off at $t = t_{ron} + t_{roff}$, the pulse reduces to a percentage of the original rate (typically

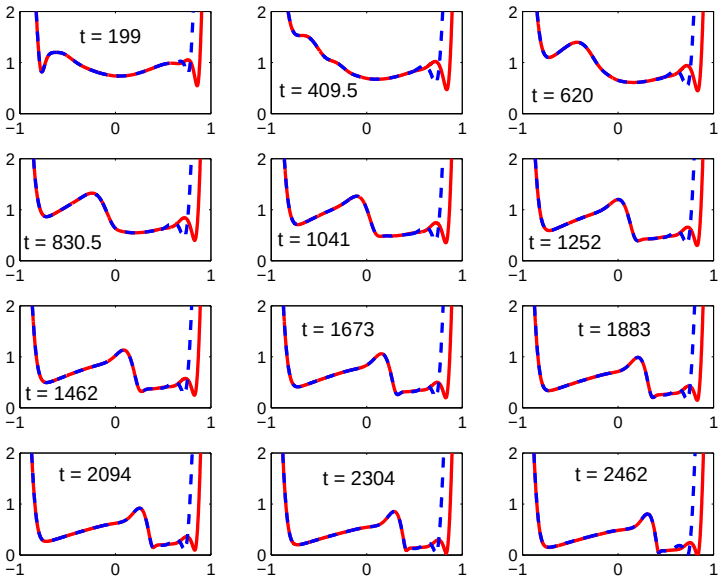

Figure 13: Relaxation after reflex tearing is turned off, $t_{ron} + t_{roff} \leq t \leq \Delta t_{co} + \Delta t_o$. All parameters are the same as in Figure 11 with $g_{top} = .50$ for dashed line and for the solid line $g_{top} = .80$ and $Q_{0r} = 2.5Q_{mT}$.

5% or 2%) for the remainder of the simulation.

Figure 15 displays the center thickness measurements of four simulations having the same parameters as in Figure 13 with $g_{top} = .80$ and $Q_{0r} = 2.5Q_{mT}$, but modified reflex tearing function as described above. In the first case, a constant influx of rate $Q_{0r} = .3125Q_{mT}$ begins at $t = t_{ron}$ and remains on throughout the entire simulation. For the second case, a constant influx of rate $Q_{0r} = 2.5Q_{mT}$ begins at $t = t_{ron}$ and at $t = t_{ron} + t_{roff}$ the influx is reduced to 5% of Q_{0r} for the remainder of the simulation. In the third case, the influx is now reduced to 2% of the rate Q_{0r} at $t = t_{ron} + t_{roff}$. Finally, the fourth case is the same as the third case except $Q_{0r} = 2.375Q_{mT}$. Table 4 summarizes the parameters for each of the cases shown in Figure 15. The modification of the reflex tearing influx does aid in leveling off the center thickness profile for long times. In all cases, the bulge of tear fluid from the upper meniscus is larger and drains down the cornea faster. Furthermore, the tear film thickness stays more or less constant in the upper meniscus for later times because there is a balance between the influx and the mass loss due to evaporation. This differs from simulations when the reflex tearing pulse is turned completely off. In those simulations,

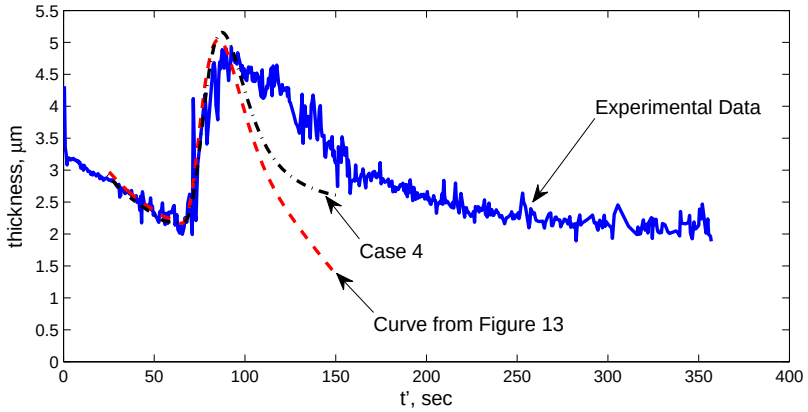

Figure 14: Single thickness measurement from the center of the cornea taken by King-Smith *et al.* (2000), the center of the cornea film thickness from Figure 13 and Case 4 simulation.

the upper-meniscus/black-line region continues to decrease as shown in panel 4 of Figure 10 due the upper meniscus continuing to draw up tear fluid. Case 4 makes the best comparison to King-Smith *et al.* (2000) measured data and is plotted in Figure 14, where it has been shifted in time to visually align with the beginning of the increase in film thickness. As before, we are limited in the total simulation time due to tear film breakup near the lower lid.

Case	Q_{0r}, $t_{ron} \leq t < t_{ron} + t_{roff}$	Percentage of Q_{0r}, $t_{ron} + t_{roff} \leq t$
1	$0.3125Q_{mT}$	100%
2	$2.5Q_{mT}$	5%
3	$2.5Q_{mT}$	2%
4	$2.375Q_{mT}$	2%

Table 4: Reflex tearing flux function parameters for the center thickness measurements in Figure 15.

The observation that an elevated film end, i.e., a meniscus, would cause localized film thinning due to capillarity was first put forward by McDonald & Brubaker (1971) and illustrated with a puddle of milk and a paper clip. In their investigation, they observed localized thinning near the lid margins in eyes and found that it could lead tear film breakup. Thus, the breakup observed in the computation may be physically realistic in some circumstances, though this is certainly not the only location where breakup can occur (Bitton & Lovasik, 1998; Liu *et al.*, 2006). The role of the black line has been taken to be a barrier to transfer of tear fluid between the film on the anterior of

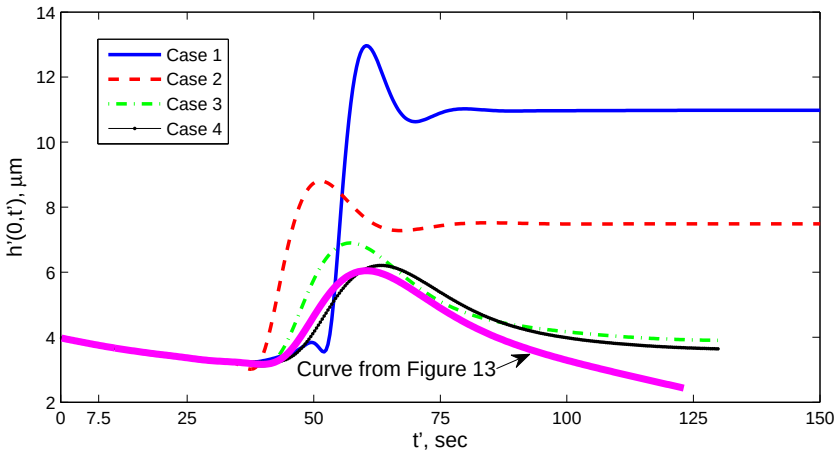

Figure 15: Film thickness at the center of the cornea for the four different cases explain in Table 4 compared with the simulation found in Figure 13.

the eye and the meniscus at the lid margin (Wong *et al.*, 1996; Sharma *et al.*, 1998). In the absence of reflex tearing, the tear film is thought to be "perched," that is, separate from the menisci (Miller *et al.*, 2002). In this last paper, Miller *et al.* (2002) assert that lid motion is required to disturb the black line and the perched tear film.

In this paper, we consider the black line in the presence of a tear supply from the lid margins, as may be expected in reflex tearing, and now the role of the black line appears to be more subtle than simply being a barrier to fluid flow. We find in our computations that the thin region at the end of the meniscus does not prevent even relatively small fluxes from the upper lid from breaching that region with a subsequent pulse or bolus of fluid propagating down the film. In order to get a good comparison for the data taken from the six minute man, a relatively large flux is used for reflex tearing which results in an appropriately sized pulse of fluid that will match the experimental rise in the center of the tear film. Thus, provided the flux is not too large (that is, γ near 2) and the flux returns to zero after the initial pulse of reflex tears, there remains a local thin region near the meniscus, but it may not be so thin that it may be termed a black line. If a nonzero flux persists after the initial pulse of reflex tears, according to our computational results, then there is not really a black line region near the upper lid after the initial pulse of reflex tears.

The flux from reflex tearing, together with gravity to help drag the fluid down the film, seems to be able to supply tear fluid through the black line region; the amount of fluid passing through

depends on the magnitude and duration of the flux, and the change in the middle of thickness of the tear film is rather sensitive to the amount of flux. When the reflex tearing is only on for a short duration, then there is only a temporary increase in the film thickness in the center of the tear film. With only a small constant reflex tear flux remaining after a brief stronger period of reflex tearing, the thickness of the tear film stabilizes at a reasonable value in comparison with experiment.

By adjusting the parameter Q_{0r}, we attempted to identify a minimum influx required to break through the black line located at the upper meniscus. In all simulations, the minimum tear film thickness in the upper meniscus region lifted up, as in panel 3 of Figure 10, during the reflex tearing influx to a thickness that depended upon Q_{0r}; tear fluid would then drain down the cornea. In some instances, when Q_{0r} was small, the draining tear fluid would not reach the center of the cornea before tear film break up occurred at the inferior black line (near $x = 1$). We note that it is unclear whether the one-dimensional findings regarding the resistance of the black lines are definitive in eyes since tear fluid entering the upper meniscus can travel either down the cornea or around the eye in the menisci, and the menisci are expected to provide less resistance to flow.

5 Conclusion

In this paper, we presented a finite-difference-based overset grid method to calculate solutions to the nonlinear tear film evolution equation. The method was verified on a simplified nonlinear test problem containing the difficult characteristics of the tear film model. The RODE approach was best at addressing the challenge of flux boundary conditions containing third derivatives. The overset grid significantly reduced the number of grid points to approximate the different regions where tear film thickness varied rapidly.

The physiological effect of reflex tearing was modeled and studied finding favorable comparisons to measured thickness data from the center of the cornea. For the evolution of the tear film, we chose the uniform stretched model first proposed by Jones *et al.* (2005) considering the effects of gravity and evaporation along with slip in an attempt to model the complex corneal surface more closely. In this study, realistic lid motion along with flux boundary conditions developed by Heryudono *et al.* (2008) were modified to include a pulse of steady influx from the lacrimal gland

attributed to reflex tearing. In a typical simulation, the upper lid opens fully; capillary-driven thinning creates the black lines at each lid; reflex tearing is turned on and tear fluid breaks through the black lines lifting the tear/air interface up at the upper and lower lid; reflex tearing is then turned off or the influx rate is reduced and gravity effects dominate in the upper meniscus causing a bulge of fluid to drain down the cornea. The tear film thickness decreases at a constant rate due to evaporation in the absence of other effects such as influx from the ends.

We studied the simulations of the tear film in the center of the cornea and identified that the decrease in the profile initially during the relaxation period was due only to evaporation effects on the time scale before reflex tearing began. The mechanism causing the sudden increase in the center of the film for later times is gravity draining the fluid from the upper meniscus down the cornea. We found that the center thickness was sensitive only to the amount of fluid in the upper meniscus after reflex tearing has been turned off. In general, less input into the upper meniscus caused a increase in capillary effects relative to the gravitational effects in the upper meniscus, resulting in a slower and smaller pulse moving down the cornea. In the simulations, we were limited to when reflex tearing was turned on due to film break up at the black lines. Also, we could not run the simulation for longer than 150s due to film break up. A reasonable next step that we have begun is to add a disjoining pressure term into the tear film model.

Comparisons with measurements made at the center of the cornea from one subject taken by King-Smith *et al.* (2000) were made. Overall, we found qualitative agreement, with our simulations able to capture almost all of the different aspects of the center thickness profile found in Figure 14 but at time scales that were shorter than those observed *in vivo*. The center thickness profile with $g_{top} = .50$ in Figure 11 provided the best comparison with regard to the formation of peak with a height increase of 2.8μm over 20.7s. One characteristic of the measured data that was missing from the first results shown was the leveling off of the tear film thickness for later times. We found that adding a small constant supply of reflex tears from the upper lid after the initial reflex pulse ($t \geq t_{ron} + t_{roff}$) caused the center thickness to level off with time. Furthermore, in all our simulations we found the flux from reflex tearing coupled with the help of gravity pulling the tear fluid down the cornea supplies fluid through the black line region.

Extension of the model to a two-dimensional eye-shaped domain will produce new insights into

the tear film formation and dynamics as well as a computational model. In particular, how the flow between the upper and lower menisci via the canthi will affect the distribution of reflex tears. Because such a model can incorporate flow between and along the menisci as well as across the anterior of eye, evaluating the propensity of the black lines to act as barriers can be more thoroughly addressed. We are currently working on a computational model via a moving overset grid method using the OVERTURE framework (Henshaw, 2002).

Acknowledgments

This work was supported in part by a grant from the National Science Foundation (DMS-0616483). The authors thank P. Fast and A. Heryudono for many helpful suggestions and discussions. We thank the referees for careful reading of the manuscript and many helpful suggestions.

A Numerical method

A.1 Composite grids

To generate the stretched grids, we created the following piecewise continuously differentiable grid stretch function of the form

$$f(x) = \begin{cases} x & \text{for } x \in [0, x_b] \\ (\frac{x-c}{a})^n + b & \text{for } x \in (x_b, x^*] \\ s(x - x^*) + x_e & \text{for } x \in (x^*, \infty) \end{cases}$$

where x_e, x_b, n and s are specified and the remaining parameters are defined as

$$a = \left[\frac{(x_e - x_b) n^{\frac{n}{n-1}}}{s^{\frac{n}{n-1}} - 1} \right]^{\frac{n-1}{n}}, \; b = x_b - \left[\frac{a}{n}\right]^{\frac{n}{n-1}}, \; c = x_b - \left[\frac{a^n}{n}\right]^{\frac{1}{n-1}} \text{ and } x^* = \left[s \frac{a^n}{n} \right]^{\frac{1}{n-1}} + c.$$

Since we are interested in stretching the boundary-fitting fine grid with spacing Δ_f into the coarse Cartesian background grid with spacing Δ_c, n must be chosen less than one. The equally spaced fine boundary-fitting grid is marked along the y-axis while the stretched grid is constructed on the

x-axis using the inverse of $f(x)$. By design, the new grid on the x-axis has spacing Δ_f on the interval $(0, x_b)$, in the transition region (x_b, x^*) the spacing changes smoothly from Δ_f to $\frac{1}{s}\Delta_f$, and on the remainder of the grid the spacing is $\frac{1}{s}\Delta_f$. We select $s = \frac{\Delta_f}{\Delta_c}$, while typically $n = 1/200$ and $x_e = .05 + x_b$. The end of the transition region x^* depends on the values chosen for n and x_e. Figure 16 illustrates the stretching of a fine grid with uniform spacing $\Delta_f = 1/20$ into a coarse grid with spacing $\Delta_c = 1/4$ using the parameters $x_b = 0.1$, $x_e = 0.2$, $n = 1/200$ and $s = 1/5$. In most cases, the resulting stretched grid is cut off after x^*, the transition region, for use in the composite grid since it provided enough overlap for explicit interpolation.

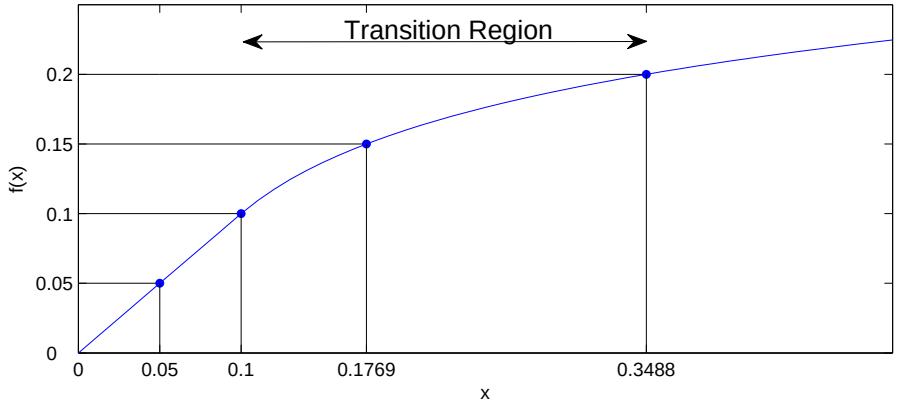

Figure 16: An example of the stretch function with parameters $x_b = 0.1$, $x_e = 0.2$, $n = 1/200$ and $s = 1/5$. Here the uniform grid with spacing $\Delta_f = 1/20$ is marked along the y-axis and the stretched grid is found along the x-axis by the inverse of $f(x)$.

A.2 Volume conservation calculation

Recall that for a particular value of time the volume of fluid defined in equation (22). The error in volume conservation for a numerically computed solution having volume $V(t)$ is

$$E_V(t) = \left\| V(t) - V_i - h_0 \left[X(t) - X(t_0) \right] + \int_{t_0}^{t} \left[Q(1,t) - Q(-1,t) \right] \, dt - \int_{t_0}^{t} \frac{1 - X(t)}{2} \int_{-1}^{1} G(\xi, t) \, d\xi \, dt \right\|_{\infty},$$

where V_i denotes the initial volume computed exactly from initial data. For the team film model, $G(\xi, t) = 0$. The integral (22) can be rewritten as the initial value problem

$$\frac{d}{d\xi}u(\xi) = \frac{1 - X(t)}{2}H(\xi, t), \quad u(-1) = 0, \quad \xi > -1, \tag{42}$$

where $V(t) = u(1)$ (Trefethen, 2000). Since at any time step the value of $H(\xi, t)$ is only known as the discrete values $\mathcal{H}$, the derivative of $u(\xi)$ is approximated by second-order accurate finite difference on a single nonuniform grid comprised of all the discretization points in each component grid, i.e., collapsing all the component grids into on single nonuniform grid. The matrix representation is

$$Cu = \frac{1 - X(t)}{2}\mathcal{H} \tag{43}$$

with $\mathcal{H} = (H(\xi_0^1) \ \ldots \ H(\xi_N^3))^T$. Thus, $V(t)$ is found by multiplication of the last row of C^{-1} with $\frac{1-X(t)}{2}\mathcal{H}$.

The error in volume conservation is tracked in the tear film model and used as a computational diagnostic tool to verify the accuracy of the scheme. To assess the reliability this tool, the maximum of the relative error and of the absolute error are compared with the error in volume conservation in Figure 17; here the nonlinear test problem is shown on a composite grid containing 3000 points. The maximum volume conservation error over time is comparable to the maximum relative error. Therefore, the error in volume conservation is a rough indicator of, but not a bound on, the maximum relative error over the simulation.

References

Berger, R. E. & Corrsin, S. 1974 A surface tension gradient mechanism for driving the pre-corneal tear film after a blink. *J. Biomechanics* **7**, 225–238.

Berke, A. & Mueller, S. 1998 The kinetics of lid motion and its effects on the tear film. In *Lacrimal Gland, Tear Film, and Dry Eye Syndromes 2* (ed. D. A. Sullivan, D. A. Dartt & M. A. Meneray), pp. 417–424. New York: Plenum.

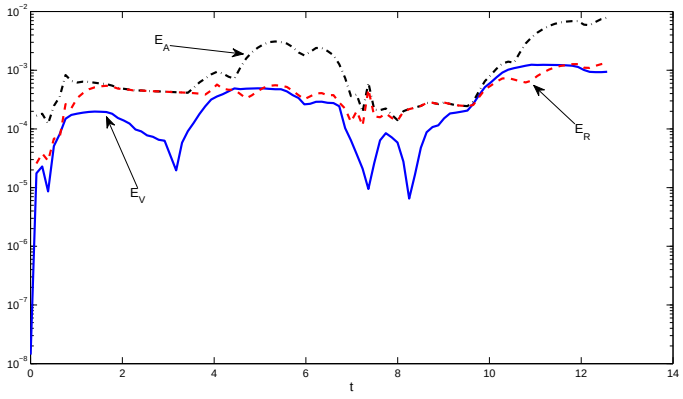

Figure 17: The maximum relative error (dashed, E_R) and maximum absolute error (dash-dot, E_A) along with the max volume conservation error (solid, E_V) calculated on a 3000 points composite grid for the nonlinear test problem over two cycles.

Berrut, J. & Trefethen, L. 2004 Barycentric Lagrange interpolation. *SIAM Review* **46**.

Bertozzi, A. L., Brenner, M. P., Dupont, T. F. & Kadanoff, L. P. 1994 Singularities and similarities in interface flows. In *Trends and Perspectives in Applied Mathematics* (ed. L. Sirovich), pp. 155–208. New York: Springer.

Bitton, E. & Lovasik, J. V. 1998 Longitudinal analysis of precorneal tear film rupture patterns. In *Lacrimal Gland, Tear Film and Dry Eye Syndromes 2* (ed. D. A. Sullivan, D. A. Dartt & M. A. Meneray), pp. 381–389. New York: Plenum Press.

Braun, R. J. 2006 Models for human tear film dynamics. In *Wave Dynamics and Thin Film Flow Systems* (ed. R. Usha, A. Sharma & B.S. Dandapat), pp. 404–434. Chennai, India: Narosa.

Braun, R. J. & Fitt, A. D. 2003 Modelling drainage of the precorneal tear film after a blink. *Math. Med. Bio.* **20**, 1–28.

Braun, R. J. & King-Smith, P. E. 2007 Model problems for the tear film in a blink cycle: single equation models. *J. Fluid Mech.* **586**, 465–490.

Chesshire, G. & Henshaw, W. 1990 Composite overlapping meshes for the solution of partial differential equations. *J. Comp. Phys.* **90**, 1–64.

Creech, J. L., Do, L. T., Fatt, I. & Radke, C. J. 1998 In vivo tear-film thickness determination and implications for tear-film stability. *Curr. Eye Res.* **17**, 1058–1066.

Diez, J. A. & Kondic, L. 2002 Computing three-dimensional thin film flows including contact lines. *J. Comp. Phys.* **183**, 274–306.

Doane, M. G. 1980 Interaction of eyelids and tears in corneal wetting and the dynamics of the normal human eyeblink. *Am. J. Ophthalmol.* **89**, 507–516.

Farris, R.L., Stuchell, R.N. & Mandel, I.D. 1981 Basal and reflex human tear analysis. i. physicial measurements: osmolarity, basal volumes, and reflex flow rate. *Ophthalmol.* **88**, 852–57.

Fast, P. & Shelley, M. J. 2004 A moving overset grid method for interface dynamics applied to non-newtonian Hele-Shaw flow. *Journal of Computational Physics* **195**, 117–142.

Haley, P. & Miksis, M. J. 1991 Effect of the contact line on droplet spreading. *J. Fluid Mech* **223**, 57–81.

Henshaw, W. D. 2002 Ogen: the Overture overlapping grid generator. *Tech. Rep.* UCRL-MA-132237. Lawrence Livermore National Laboratory.

Heryudono, A., Braun, R. J., Driscoll, T. A., Maki, K. L., Cook, L. P. & King-Smith, P. E. 2008 Single-equation models for the tear film in a blink cycle: realistic lid motion. *Mathematical Medicine and Biology* **24**, 347–377.

Jensen, O. E. & Grotberg, J. B. 1993 The spreading of heat or soluble surfactant along a thin liquid film. *Phys. Fluids A* **5**, 58–68.

Johnson, M. E. & Murphy, P. J. 2006 Temporal changes in the tear menisci following a blink. *Exp. Eye Rsch.* **83**, 517–525.

Jones, M. B., Please, C. P., McElwain, D. S., Fulford, G. R., Roberts, A. P. & Collins, M. J. 2005 Dynamics of tear film deposition and drainage. *Mathematical Medicine and Biology* **22**, 265–288.

King-Smith, P.E., Fink, B.A., Hill, R.M., Koelling, K.W. & Tiffany, J.M. 2004 The thickness of the tear film. *Curr. Eye Res.* **29**, 357–68.

King-Smith, P.E., Fink, B.A., Nichols, K.K., Hill, R.M. & Wilson, G.S. 2000 The thickness of the human precorneal tear film: evidence from reflection spectra. *IOVS* **40**, 3348–59.

Liu, H., Begley, C. G., Chalmers, R., Wilson, G., Srinivas, S. P. & Wilkinson, J. A. 2006 Temporal progression and spatial repeatability of tear breakup. *Optom. Vis. Sci.* **83**, 723–730.

Madsen, N. K. & Sincovec, R. K. 1979 Algorithm 540: Pdecol, general collocation software for partial differential equations. *ACM TOMS* **5**, 326–351.

Maitchouk, D.Y., Beuerman, R.W., Ohta, T., Stern, M. & Varnell, R.J. 2000 Tear production after unilateral removal of the main lacrimal gland in squirrel monkeys. *Arch. Ophthalmol.* **118**, 246–52.

Mathers, W.D. 1993 Ocular evaporation in meibomian gland dysfunction and dry eye. *Ophthalmology* **100**, 347–351.

Maurice, D. M. 1973 The dynamics and drainage of tears. *Intl. Ophthalmol. Clin.* pp. 103–116.

McDonald, J.E. & Brubaker, S. 1971 Meniscus-induced thinning of tear films. *Am. J. Ophthalmol.* **72**, 139–146.

Miller, K. L., Polse, K. A. & Radke, C. J. 2002 Black-line formation and the perched human tear film. *Curr. Eye Rsch.* **25**, 155–162.

Mishima, S., Gasset, A., Jr., S. D. Klyce & Baum, J. L. 1966 Determination of tear volume and tear flow. *Invest. Ophthalmol.* **5**, 264–276.

Shampine, L., Reichelt, M. & Kierzenka, J. 1999 Solving index-1 DAEs in matlab and simulink. *SIAM Review* **41**.

Sharma, A., Tiwari, S., Khanna, R. & Tiffany, J.M. 1998 Hydrodynamics of meniscus-induced thinning of the tear film. In *Lacrimal Gland, Tear Film, and Dry Eye Syndromes 2* (ed. D. A. Sullivan, D. A. Dartt & M. A. Meneray), pp. 425–431. New York: Plenum Press.

Steger, J. L. & Benek, J. A. 1987 On the use of composite grid schemes in computational aerodynamics. *Computer Methods in Applied Mechanics and Engineering* **64**, 301–320.

Trefethen, L.N. 2000 *Spectral Methods in* Matlab. Philadelphia: SIAM.

Volkov, P. A. 1966 A finite difference method for finite and infinite regions with piecewise smooth boundaries. *Doklady* **168**, 744–747.

Volkov, P. A. 1968 The method of composite meshes for finite and infinite regions with piecewise smooth boundaries. *Proceedings of the Steklov Institute of Mathematics* **96**, 145–185.

Witelski, T. P. & Bowen, M. 2003 Adi schemes for higher-order nonlinar diffusion equations. *Appl. Numer. Math.* **45**, 331–351.

Wong, H., Fatt, I. & Radke, C.J. 1996 Deposition and thinning of the human tear film. *J. Colloid Interface Sci.* **184**, 44–51.

Ye, Y. & Change, H. 1999 A spectral theory for fingering on a prewetted plane. *Phys. Fluids* **11**, 2494–2515.

Yeo, Y. L., Craster, R. V. & Matar, O. K. 2003 Marangoni instability of a thin liquid film resting on a locally heated horizontal wall. *Phys. Rev. E* **67**, 056315.

Zhornitskaya, L. & Bertozzi, A. L. 2000 Positivity-preserving numerical schemes for lubrication-type equations. *SIAM J. Numer. Anal.* **37**, 523–555.

List of Tables

List of Figures